Experimental Investigation of the Homogeneous Freezing of Aqueous Ammonium Sulfate Droplets

Ben H. Larson and Brian D. Swanson*

Department of Earth and Space Sciences, Box 351310, University of Washington, Seattle, Washington 98195

Received: August 2, 2005; In Final Form: October 25, 2005

We have measured the light scattering intensity and homogeneous ice nucleation temperatures from water droplets containing 0−33 wt % ammonium sulfate. In these laboratory experiments, we used a free-fall freezing tube technique to determine the fraction of frozen droplets at a particular droplet temperature by measuring the depolarized light scattering intensity from the droplets in free-fall. Previously reported freezing temperatures for solution concentrations greater than 5 wt % display a larger spread than can be accounted for by the reported experimental errors. We find freezing temperatures in good agreement with the lowest temperature freezing results reported by previous experiments. Our ammonium sulfate freezing temperature data set with water activity less than 0.98 is consistent with a curve that deviates in activity shift by about 5% from the best-fit ice nucleation temperature versus water activity curve found by Koop et al. in 2000, but the significance of this deviation will only be known with further high-precision ice nucleation temperature measurements for other aqueous solutions.

1. Introduction

Ice in upper-tropospheric clouds (1) influences the Earth's climate by scattering and absorbing radiation,[1] (2) is the major source of the Earth's precipitation,[2] and (3) is the substrate where much of the heterogeneous chemistry leading to tropospheric ozone depletion occurs[3]. Ice initiation in upper-tropospheric clouds is difficult to model because of our lack of knowledge of the microphysical parameters that characterize ice nucleation processes and the spatially and temporally varying conditions in clouds such as temperature, saturation ratio, cloud particle composition, and the presence or absence of ice nuclei (IN). Ice initiation can occur in the upper troposphere at higher temperatures and low ice saturation ratios via heterogeneous nucleation due to the presence of IN (e.g., mineral dust). But, in the absence of heterogeneous processes, air parcels containing droplets of aqueous sulfate or sulfuric acid solutions either partially or fully neutralized by ammonia to ammonium sulfate can rise and cool. These droplets are hygroscopic and adjust their composition (becoming more dilute or concentrated) to keep their water vapor pressure in equilibrium with ambient conditions. As temperatures decrease, droplets supercool and may homogeneously freeze or may remain in this metastable liquid state dependent upon whether they reach a sufficiently low temperature.[4−11]

In this laboratory study, we investigate the formation of ice particles from aqueous ammonium sulfate, $(NH_4)_2SO_4-H_2O$, solution droplets using a droplet free-fall freezing tube (FFFT) technique. In our technique, droplets with well-known solution concentrations are emitted and cool as they fall down the axis of a freezing tube. The fractions of droplets that are liquid and solid at various heights (temperatures) are measured by detecting the amount of depolarized light scattered into two orthogonal directions. This methodology has the advantage of following the droplet's trajectory throughout the homogeneous freezing process without potential droplet−droplet, droplet−aerosol, or droplet−substrate interaction effects. Also, our droplet phase detection method is similar to the techniques used in remote-sensing lidar[12] except we measure both total and depolarized light scattering intensity, while typical lidar measures the polarized and depolarized signals.

Six laboratory investigations have been conducted in recent years to measure the dependence of freezing temperature of $(NH_4)_2SO_4-H_2O$ solution droplets on solute concentration. The published ice nucleation temperatures from these experiments do not agree within the reported experimental errors. For example, at an $(NH_4)_2SO_4$ concentration of 30 wt %, the reported freezing temperatures vary by over 15 °C.[13−19] For regions of the upper troposphere containing highly concentrated $(NH_4)_2SO_4$ droplets, it is important to determine whether ice nucleation occurs at −45 °C or −60 °C to accurately model cloud formation and cloud-particle light-scattering properties.

The previous $(NH_4)_2SO_4$ ice nucleation experiments employed different techniques, observation times, particle sizes, and sensitivities, but efforts to determine whether the previous results are consistent with one common intrinsic volume nucleation rate have not been successful.[18,19] Four of the experiments used aerosol flow tubes (AFT) coupled with infrared spectroscopy detection methods.[14−16,18] One group used optical microscopy (OM) and differential scanning calorimetry (DSC) techniques.[13] Another investigation employed a continuous flow thermal diffusion chamber (CFDC).[17] Several experimenters reported drawbacks in these various techniques: Some AFT experiments encountered difficulties constraining the aerosol composition—both in concentration and phase.[18] Often, in the flow tube, the $(NH_4)_2SO_4$ particles would effloresce, giving a false positive freezing signal. The DSC experiments required suspending the droplets in an oil emulsion, while the OM technique involved placing the droplets on a hydrophobic microscope slide.[13] The extent to which potential surface processes influence the freezing of small-sized droplets remains unclear[20−22] despite a recent study [23] of the freezing of larger-sized pure water droplets.

* Corresponding author e-mail address: brian@ess.washington.edu.

10.1021/jp054270l CCC: $33.50
Published on Web 01/10/2006

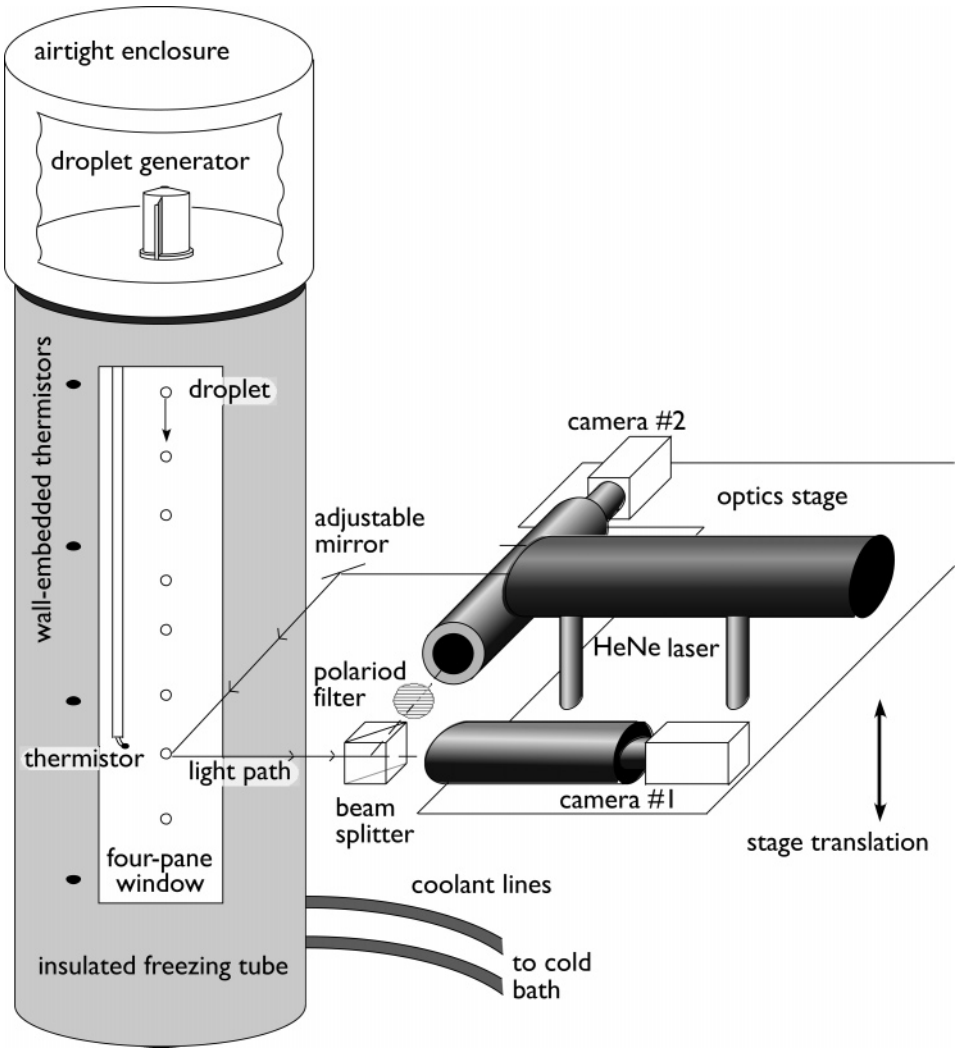

Figure 1. Schematic drawing of droplet free-fall freezing tube apparatus.

2. FFFT Apparatus and Procedure

Early experiments measuring ice nucleation in free-falling droplets used either a long column of nitrogen gas,[24] a cold chamber,[25] or a cooled tube.[26] The FFFT technique we use was developed by Wood et al.[27] The experimental apparatus (shown schematically in Figure 1) consists of a droplet-on-demand droplet generator mounted coaxially on top of a 50-cm-high hollow cylinder. The temperature gradient along the tube axis (for the experiments reported here, (dT/dz) ranged from 0.8 to 1.8 °C/cm depending upon the freezing temperature of interest) is established by circulating cold methanol through copper coils attached to the tube base. To operate at the low freezing temperatures of $(NH_4)_2SO_4-H_2O$ solutions, the freezing tube's insulation was increased over previous experiments,[27] and the two large observation windows on either side of the tube were replaced with four-pane versions. Reservoirs at two heights inside the tube were added, and water was injected into both reservoirs and onto the tube bottom before cool-down and beginning the experiments. The reservoirs stabilized the tube wall humidity and eliminated nearly all droplet evaporation (and temperature lag effects) reported in our previous experiments.[27]

The droplet phase detection system consists of two video cameras with telemicroscopic lenses, a polarizing filter, and a beam splitter mounted on a metal stage which, after alignment, may be translated up and down along the freezing tube's vertical axis (see Figure 1). To determine the fraction of frozen droplets at a particular temperature, we position the phase detection system such that a polarized HeNe laser beam intersects the droplet stream at the height of interest. Using the two cameras (one without and one with a polarizer) viewing the droplet stream through the beam splitter, we obtain streak images of both the total, TSL, and depolarized, DSL, scattered light intensity from each falling droplet. A video screen splitter allows us to simultaneously display side-by-side (and record on videotape and computer) the images from the two cameras. To quantitatively compare the scattering intensity from two different streaks, we calibrated the two cameras to correct for the relative sensitivities of each camera and the transmission efficiency of the polarizing filter. We also closely monitored the scattered light intensity and dynamic range of our digitizing system to confirm that the streaks were never bright enough to saturate the camera or the frame grabber.

For the experiments reported here, 15−25-μm-radius droplets were emitted at a rate of about 5 Hz, and each data run began by first translating the detection stage to find the rough 50% frozen fraction height. The stage was translated down to where 100% of the particles were frozen, and measurements were made at different heights by moving the stage at approximately 0.15 °C intervals along the tube until the 0% frozen level was reached. For each height, 2−3 min of streak data were collected and subsequently digitized to measure the intensity of the images of individual droplet streaks. Each experiment typically yielded

200−400 droplet measurements at a single temperature (height in the tube) and 3000−4000 droplet measurements overall for a single frozen-fraction curve measurement with the average total streak brightness typically ranging 10−50% of the 8-bit full-scale value. For each droplet streak, we determine the ratio DSL/TSL while accounting for background light intensity present in each frame by sampling dark screen locations near the streaks and subsequently subtracting the associated background light intensity from each streak intensity. The TSL streaks were always bright, with average intensities well above the detection threshold. The DSL streaks, however, were sometimes faint enough that the background light intensity would make identification difficult. Typically, the background light intensity, which appears as white speckles on the video image, approached 4% of the full-scale brightness. From repeated analysis, we found we could reliably identify a streak with an average intensity of about 5% of full scale, but no less. In the cases where the depolarized streaks were indistinguishable from the background light intensity in the frame (i.e., a brightness of 5% or less), they were assigned an intensity of zero.

Samples of solutions with various concentrations were prepared by mixing high-purity liquid chromatography (HPLC) grade water with 40 wt % $(NH_4)_2SO_4$ (99.99% pure) from Aldrich Chemical. The dilutions were typically mixed to better than 0.05 wt % accuracy. For each data run, the appropriate concentration solution was injected into a new (HPLC water rinsed and cleaned) droplet generator cartridge and immediately placed atop the freezing tube inside a sealed airtight enclosure. The enclosure and freezing tube was then purged of aerosol-laden room air using nitrogen gas, thus eliminating the potential problem, especially at colder temperatures, of an occasional influx of aerosol particles inducing droplet freezing through contact nucleation. Droplet solution concentration appears to remain constant throughout an experiment. The bulk liquid in a cartridge remains in contact with a well-mixed reservoir before ejection, and the amount of fluid ejected over a data run (3000−4000 droplets) is less than 4 μL—a miniscule fraction of the total 5 mL fluid reservoir. We checked for systematic changes in droplet freezing temperature over the course of a data run and also for variability in freezing temperatures extracted from repeat measurements with different cartridges, but none were found. Freezing tube temperatures were regularly recorded via computer using thermistors embedded in the cylinder walls and a thermistor attached to the bottom of a movable glass rod, which can be positioned at any level vertically in the air (within a few millimeters) adjacent to the droplet stream. (A 0.1 °C correction to our air thermistor reading was made to account for self-heating and the small amount of heat conduction through the manganin wire thermistor leads, which are at room temperature about 50 cm from the thermistor.) Typically, the wall temperature changed no more than a few hundredths of a degree every hour. Since we could not measure the droplet temperature or chamber humidity versus height directly, we developed a computer model (after the model described in Wood et al.[27]) to calculate the droplet temperature. The inputs to this model were the temperatures of the tube walls, the air temperature at various heights in the tube close to the droplet stream, and the droplet sizes (from strobe video-microscopy shadow images) taken during the experiments at various heights in the droplet stream.

Growth or evaporation during free-fall can change the droplet temperature and composition. A standard Maxwell-type model has been used to calculate the temperature and radius of a droplet as it falls through the temperature and humidity gradient in the freezing tube.[27] The shadow images of the droplets taken during free-fall show little change in droplet size (less than 2 μm—our droplet size resolution limit), and hence, the droplet temperature correction due to droplet size changes was quite small (<0.1 °C) for most droplets. During experimental runs, we did not image the droplets in the first few centimeters after droplet generator emission; however, subsequent installation of an upper window in the chamber and measurements conducted after the data set was collected suggest that the droplet size is constant here as well. Since droplet volume changes were less than 10% during the transit of the tube, we are confident that the droplet composition remains relatively constant (maximum composition change for a 10% volume change is 4 wt % for the most concentrated solutions measured here). Further discussion of the analysis and experimental details can be found in refs 27 and 28.

3. Results

3.1. Light Scattering Intensity Results. Figure 2 displays the results for the ratio of depolarized to total scattered light intensity (DSL/TSL) for streak images from pure water droplets and 33 wt % $(NH_4)_2SO_4$ droplets. Similar data for other concentrations were collected but are not shown here. In these plots, each small gray diamond indicates the ratio of DSL/TSL for a single droplet at the temperature listed below the bin. The width of the columns vary depending on the number of droplets measured at a given temperature.

A streak in both the TSL and DSL images usually indicates the particle is frozen, while a streak in only the TSL image indicates the droplet is liquid. In general, it can be seen that DSL/TSL is small for high-temperature liquid droplets, then increases and saturates at a large average value for low-temperature frozen droplets. This behavior is well-understood and explained by the fact that scattered light from spherical liquid droplets remains polarized in the laser's original plane of polarization, but once a droplet is frozen, some of the backscattered light will be depolarized because of droplet asphereicity, cracks, bumps, surface roughness, and birefringence. We also observe that that varies considerably within any one bin—particularly for frozen droplets. This is presumably due to variations in droplet asphericity, number of cracks or bumps, and height of any surface roughness present. We find that it is rare (only about 1% of the time) for the signal to be larger than 0.5, indicating that it is highly unlikely for nearly spherical newly frozen droplets to depolarize and scatter more than half of the total scattered light intensity.

At higher temperatures, the depolarized streak is often indistinguishable from the background light intensity (such streaks are assigned zero intensity and are plotted as zero on the *x*-axis). We also find that some high-temperature droplets scatter faint streaks of depolarized light (see highest temperature bins in Figures 2 and 3). Some of these higher-temperature droplets scatter as much as 20% of the total depolarized light intensity scattered by frozen particles, which is remarkable and unexpected. Some of this depolarized scattering may be due to misalignment of our optical lenses, but we have no evidence that this is the case. A second possibility is that even at high temperatures there is a possibility that some droplets are frozen, although the predicted homogeneous nucleation rate is not high enough to account for this amount of ice nucleation at these temperatures and droplet sizes. Heterogeneous freezing is also a possibility, but the magnitude of the depolarization signal is never as large as that found for frozen droplets at lower temperatures. Another cause might be droplet asymmetry due

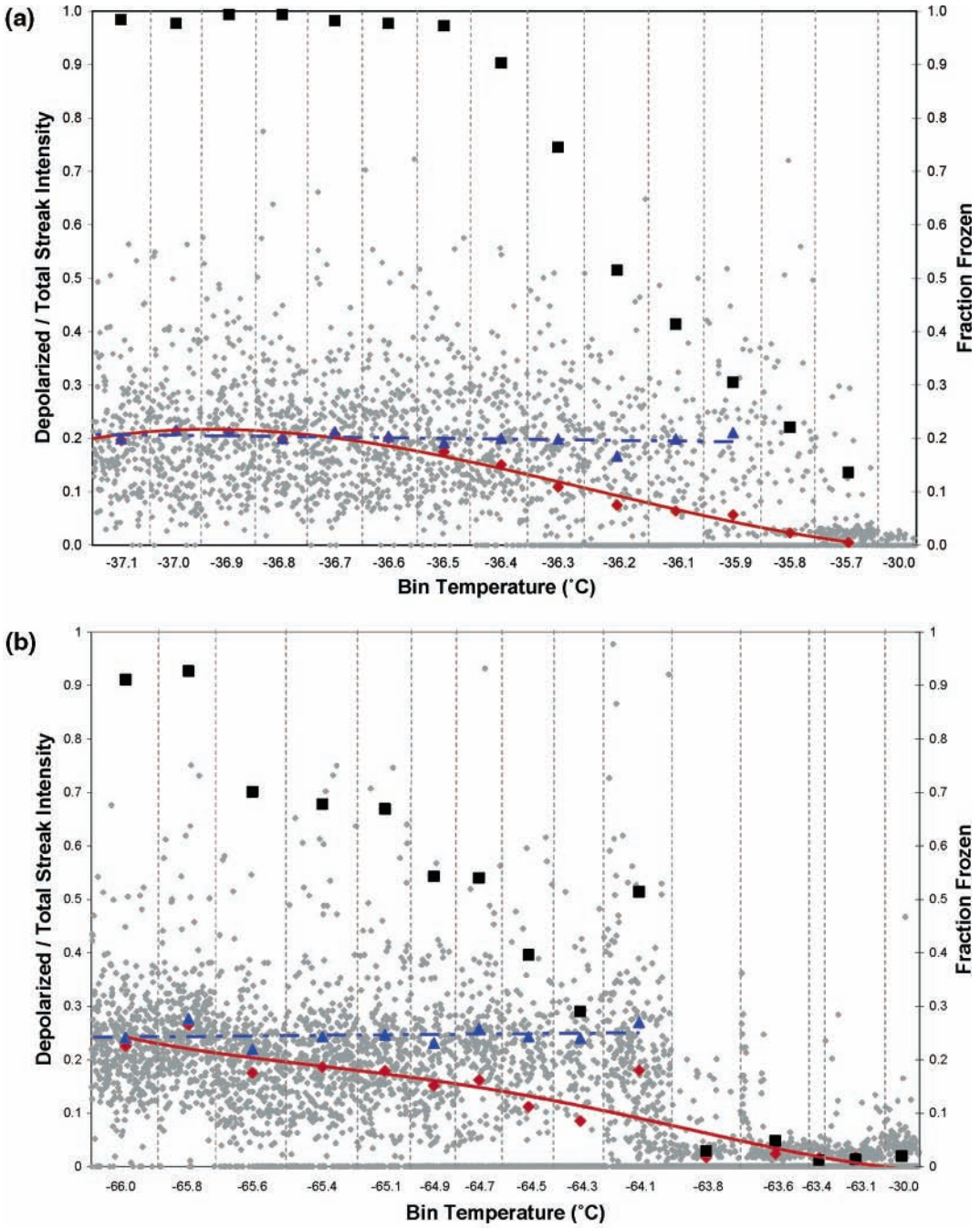

Figure 2. (a) Depolarized light scattering intensity ratio from pure water droplets. The vertical dashed lines are separations between the various temperature bins (all small ◆ in a bin are the DSL/TSL ratio for a single droplet at the respective bin temperature). In the center of each bin is plotted the fraction of frozen droplets (black square), the average scattering intensity ratio for all particles (red diamond), and the average intensity ratio for solid particles only (blue triangle). The solid and dashed lines through these points serve simply to guide the eye. (b) Same data for 33 wt % $(NH_4)_2SO_4-H_2O$ solution droplets.

to the droplet emission process inducing shape oscillations or some shape distortion due to drag when falling through air, but droplet asymmetry is predicted to be quite small for this size droplet.[29]

Since DSL/TSL is sometimes nonzero for higher-temperature (apparently liquid) droplets, we set a minimum, nonzero depolarized signal strength, or threshold value, that separates liquid from frozen droplets. We set this threshold signal by varying DSL/TSL from 0.03 to 0.11 for the various data sets and selected a value that required the droplets to be all liquid at high temperature and all solid at temperatures far below the nucleation temperature (essentially at the lowest temperatures at the bottom of tube). Once the threshold was determined, we obtained the frozen fraction $F(T)$ by counting the number of droplets with DSL/TSL above and below the threshold value (near 3% in the Figure 2 case of pure water droplets).

$F(T)$, the average DSL/TSL for all droplets, and the average DSL/TSL for frozen particles only are plotted at the center of each bin in Figure 2. The pure water case, for which the largest amount of low-temperature data were collected, most clearly demonstrates the observed trend that, as more particles become frozen, the average DSL/TSL increases, approaches a maximum, and levels off to a near constant value at which most of the particles are frozen. This trend indicates that as droplets freeze at lower temperatures they apparently "saturate" in the amount of internal disorder and surface roughness they have and that

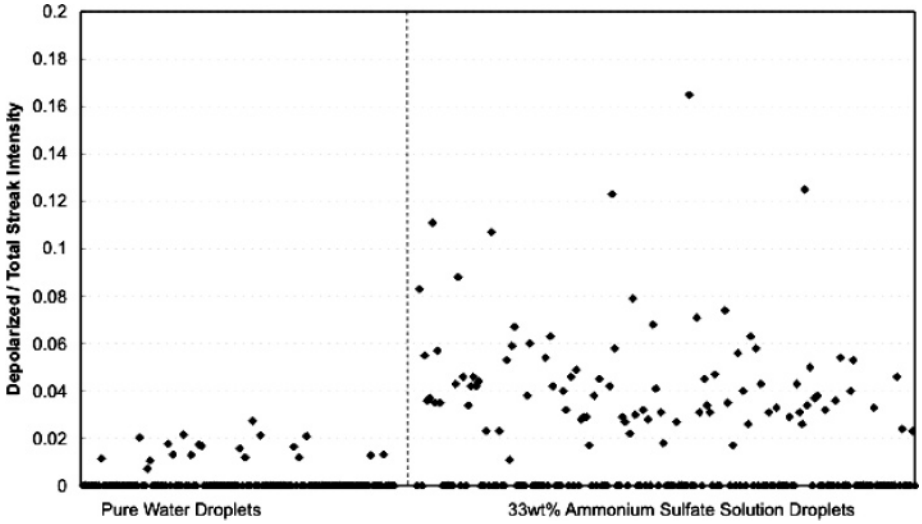

Figure 3. DSL/TSL ratio for pure water and 33 wt % $(NH_4)_2SO_4$ solution droplets near −30 °C. Each ◆ is the DSL/TSL ratio for a single droplet with droplet temperature such that $F(T) \ll 0.01$ (also see warmest temperature bin in Figure 2a,b).

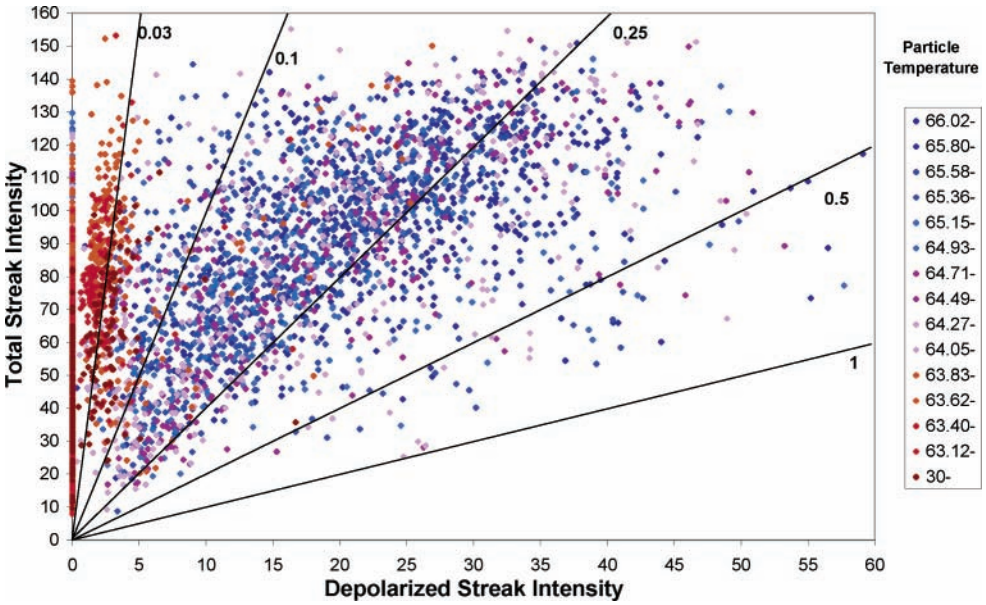

Figure 4. Depolarized and total streak intensity for 33 wt % $(NH_4)_2SO_4$ droplets with color coding corresponding to droplet temperature. The intensity units are 0−255 with 255 being the most intense scattering.

after they freeze the amount of internal disorder and surface roughness apparently does not increase as they cool to lower temperature (at least for the short times after freezing we observe here). The triangles do not extend to the far right of the plots, because at higher temperatures, too few of the droplets froze to produce a meaningful average.

Three other observations stand out in Figures 2 and 3. First, the liquid-phase DSL/TSL signal ratio (excluding those particles with a depolarized streak indistinguishable from the background) was always noticeably larger for $(NH_4)_2SO_4$ solution droplets than for pure water (see Figure 3). The ratio DSL/TSL averaged about 0.02 for pure water and ∼0.05 for 33 wt % $(NH_4)_2SO_4$ solution droplets. Second, the number of high-temperature droplets exhibiting a nonzero DSL/TSL ratio was greater for solutions than for pure water—16% for pure water and 46% for 33 wt % solution droplets. The cause of this is unclear, but experiments to measure the optical activity of supercooled $(NH_4)_2SO_4$ solutions are suggested. Third, the average DSL/TSL ratio for the frozen particles (triangles on the graph in Figure 2) was larger for frozen $(NH_4)_2SO_4$ solution particles. For example, 33 wt % frozen $(NH_4)_2SO_4$ solution particles averaged DSL/TSL ≈ 0.25 and frozen water DSL/TSL ≈ 0.20. The larger DSL/TSL ratio for the frozen $(NH_4)_2SO_4$ solution particles presumably comes from an enhanced asphericity, more cracks or bumps, larger surface roughness, the formation of solid $(NH_4)_2SO_4$, or increased birefringence and internal disorder induced by the presence of the newly formed concentrated regions of solute within the frozen droplets. As the solution concentration increases, the amount of supercooling required to initiate freezing is greater and may also lead to a more rapid or violent freezing process. This process could induce larger surface deformations or crystal disorder. Since ice excludes impurities as it freezes, an increase in solute concentration may change the solid particle morphology and the number and/or size of grains and grain boundaries within the frozen droplet.

Figure 4 shows another way to visualize the DSL/TSL ratio data for liquid and solid 33 wt % $(NH_4)_2SO_4$ droplets. Here, the depolarized streak intensity is plotted on the *x*-axis and the corresponding total streak intensity on the *y*-axis. The higher-temperature particles, with 10% or less frozen fraction, are reddish, while the lower-temperature, 60% or higher frozen fraction bins, are bluish. Purple points are intermediate tem-

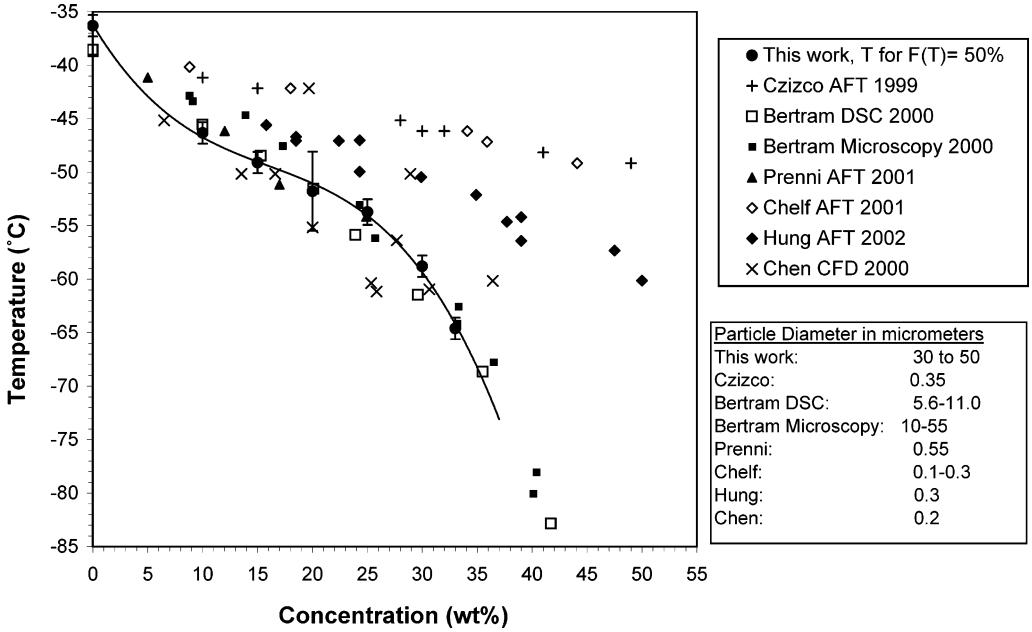

Figure 5. $(NH_4)_2SO_4-H_2O$ Droplet Nucleation Temperatures. The ● plotted here are our $(NH_4)_2SO_4-H_2O$ solution data for T_f (temperature of 50% frozen fraction). The solid line is the best-fit polynomial parametrization of the data (see eq 7). Also shown are the results from recent laboratory experiments: Czizco et al.,[15]; Bertram et al.,[13]; Prenni et al.,[16]; Chelf et al.,[14]; Hung et al.,[18]; Chen et al.[17] (1% activation level).

perature particles. The radial lines indicate constant DSL/TSL ratios. Two lobes are evident in Figure 4: a red lobe of liquid droplets with low DSL/TSL ratio, and a more spread-out blue lobe of solid particles with a higher DSL/TSL ratio. We expect the greater range of DSL/TSL ratios for solid particles, because they are not nearly as uniform as the liquid droplets. On the *y*-axis, one sees the same particles that appear at the bottom of the graph in Figures 2−3; these particles exhibit little to no depolarization and are indistinguishable from the background light intensity. Finally, the relatively open space between the red and blue lobes indicates the location of the threshold value we use in determining the cutoff between liquid and solid particles.

3.2. Freezing Temperature Results. Repeated measurements of $F(T)$ have been made for droplets with $(NH_4)_2SO_4$ concentrations from 0 to 33 wt %. We extract T_f (the temperature where 50% of the droplets are frozen) from $F(T)$ and plot these results in Figure 5 along with the results from other recent laboratory experiments. The line in Figure 5 is the best-fit simple polynomial parametrization of $T_f(x)$. The typical error bars of ±1 °C shown in Figure 5 are primarily due to uncertainty in determining the actual droplet temperature using the droplet temperature model as discussed in section 2.3. Repeated $F(T)$ measurements (two each) were made at 0, 10, 25, and 30 wt %, and the respective extracted T_f values agree within a few tenths of a degree—hence the small error bars for these points. The three independent $F(T)$ measurements made for 20 wt % concentration agree less well, as indicated by the error bars for this point in Figure 5, and our measurements of particle size changes and reasonable assumptions for the tube humidity conditions do not explain this spread.

4. Analysis

4.1. Ice Nucleation Models. In recent years, several new ideas for the phase diagram of water and the mechanism of ice nucleation have been explored (see refs 30−35 and references therein). These ideas challenge the classical model for ice nucleation and make apparent its shortcomings; the important parameters in the classical model are difficult to measure directly with sufficient precision to provide an actual prediction of ice nucleation temperature versus solute concentration. One interesting idea published in a paper by Koop et al.[33] states that, when solution concentrations are converted to water activities, a_w, both the melting temperature, T_m, and the freezing temperature, T_f, of a number of aqueous solutions fall on two distinct but "universal" curves—curves independent of solute type. Furthermore, both the T_m and T_f data appear to follow a single similarly shaped temperature versus a_w curve, only shifted in a_w by an amount Δa. This link between melting and freezing is both intriguing and puzzling, since the melting of ice is thought to be an equilibrium first-order phase transition while ice nucleation is considered to be a kinetic nonequilibrium process. But the strength of this approach is that it provides a solute-independent prediction for ice nucleation temperature versus solute concentration, which is difficult to obtain from the classical model. The theoretical foundation for this behavior is missing, but one important aspect of the work reported here is testing this idea using a new experimental methodology to determine to what extent the predicted solute independence holds for various solutes.

In general, we present our $(NH_4)_2SO_4$ freezing results in terms of a frozen fraction curve $F(T)$, the percentage of droplets frozen at temperature T [°C], and throughout, we use the term "freezing temperature" (T_f) to mean the temperature where 50% of the droplets in a uniformly sized droplet population are frozen. (The issue of freezing temperature dependence on droplet size is discussed below in conjunction with our comparison with other data.) In our experiment, we measure $F(T)$ directly and extract the nucleation rate, $J(T)$ (the rate at which ice nucleation occurs in droplets, for a given droplet population, with units of [m^{-3} s^{-1}]), by inverting

$$F(T) = 1 - \exp\left[\frac{-V_d}{\dot{T}} \int_0^T J(T')\, dT'\right] \qquad (1)$$

where V_d is the droplet volume and $\dot{T} = (dT/dz)v_{term}$ is the

cooling rate (here, (dT/dz) is the temperature gradient experienced by a droplet when falling down the freezing tube, and v_{term} is the droplet's terminal velocity). Following the method of Flagan and Seinfeld,[36,37] we calculate the terminal velocity with the relation $v_{term} = \mu\{\mathrm{Re}\}/\rho_{air}D_p$, where D_p is the particle diameter, μ the air viscosity, ρ_{air} the air density, and Re the Reynolds number, as given by ref 29.

We will make a comparison with two formulations for $J(T)$. In the case of the classical model, the precise formulation of the nucleation rate function differs among authors, although all relate $J(T)$ exponentially to two energy quantities, the activation energy for the transport of molecules across the liquid−solid-phase boundary, ΔF_{act}, and the formation energy for the critically sized ice germ, ΔF_{germ}

$$J(T) = C(T)\exp[(-\Delta F_{act} - \Delta F_{germ})/kT]^{29,38} \quad (2)$$

where, $C(T)$, the preexponential factor, contains the attack frequency, droplet size dependence, the interfacial energy of the ice−water boundary, $\sigma_{i/w}$, and other quantities dependent on the physical properties of water. k is Boltzmann's constant. In this expression, the formation energy, in turn, may be related to the germ radius, r_{germ}, and

$$\Delta F_{germ} = \frac{4}{3}\pi {r_{germ}}^2 \sigma_{i/w} \quad (3)$$

As alluded to above, the most problematic unknown quantities are $\sigma_{i/w}$ and ΔF_{act}, whose values are required to fully test the theory; so, a direct prediction of $F(T)$ is not available, since these quantities have yet to be measured directly.[29−31,39]

In contast to the classical model, the power of the translated melting-point curve (TMPC) idea is that it makes an explicit prediction for T_f for solutions with various a_w. The idea begins with the melting point curve $a_{w-m}(T) \equiv a_w(T_m)$, which can be parametrized as[33,40]

$$a_{w-m}(T) = \exp\left[15.8083 + 25301.4T^{-1} - 399752T^{-2} - 5018.85\frac{\ln(T)}{T}\right] \quad (4)$$

(where T is the temperature in K). This parametrization is consistent with melting point data from 18 different aqueous solutions in equilibrium with ice with solute molality ranging from 0 to 20 mol/kg.[33] The freezing point curve $a_{w-f}(T) \equiv a_w(T_f)$ is then defined by translating the melting point curve by a constant offset in a_w as given by $a_{w-f}(T) = a_{w-m}(T) + \Delta a$ with the offset value $\Delta a = 0.305$ selected such that $a_{w-f}(T)$ intersects the point ($a_w = 1$, $T = 235$ K), a measured freezing temperature for 1-μm-sized pure water droplets.[33]

4.2. Data−Model Comparison. Figure 6 displays $F(T)$ for three data sets with concentrations $x = 0$, 15, and 33 wt %. The lines in Figure 6a are the best fit to logistical growth model parametrization

$$F(T, x) = 1 - \frac{1}{1 + e^{-A(x)t}} \quad (5)$$

with $t = T - T_f(x)$. In this model, $T_f(x)$ is the 50% frozen fraction freezing temperature for each $(NH_4)_2SO_4$ concentration, x, in fractional weight percent, and $A(x)$ is a tunable parameter. From these fits, one finds that the slope of $F(T, x)$ at $t = 0$ decreases as x increases. The temperature range over which 33 wt % solutions go from 10% frozen to 90% frozen is more than 2 °C, while for pure water, it is less than 1 °C.

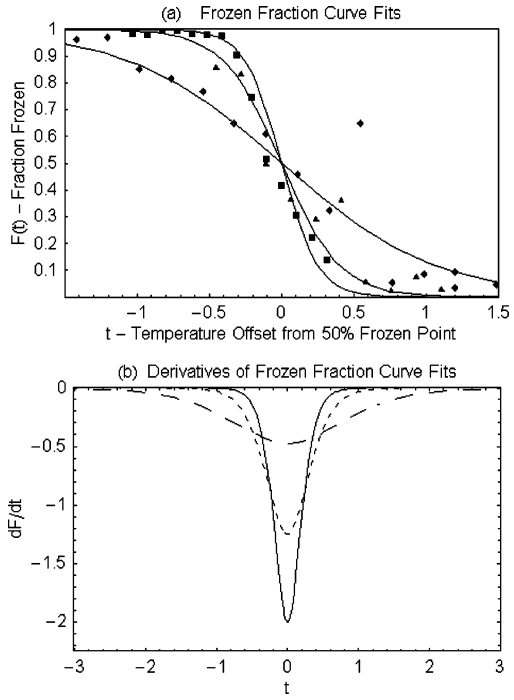

Figure 6. $(NH_4)_2SO_4$−H_2O frozen fraction curve comparison. (a) Frozen fraction data and fits (solid lines using eq 5) to our data for pure water, ■; 15 wt %, ▲; and 33 wt %, ◆. Data and fit lines are each shifted by their respective nucleation temperatures, T_f. (b) Plot of the derivative of the best-fit frozen fraction curves d$F(T)$/dT for pure water, —; 15 wt %, - - -; and 33 wt % $(NH_4)_2SO_4$, — — —.

The resulting $A(x)$ and $T_f(x)$ values result from fits of each individual data set to eq 5. A best-fit polynomial parametrization for the entire data set was then determined

$$A(x) = 4.9 - 1.1x - 30x^2 \quad (6)$$

$$T_f(x) = -36.2 - 170x + 842x^2 - 1770x^3 \quad (7)$$

where the 1σ errors in $A(x)$ and $T_f(x)$ are ±1.4 and ±0.9, respectively. The best-fit simple polynomial parametrization of $T_f(x)$ with best-fit parameters given by eq 7 are plotted as the line in Figure 5. Figure 6b plots $F' = (\mathrm{d}F/\mathrm{d}T)$ for the data shown in Figure 6a, clearly indicating the decrease in slope at $F(T = T_f)$ with increasing $(NH_4)_2SO_4$ concentration.

Using the eq 5 parametrization of $F(T, x)$, we derive $J(T, x)$ for each $(NH_4)_2SO_4$ concentration

$$J(T, x) = \frac{-\dot{T}}{V_d}\frac{A(x)}{1 + e^{A(x)t}} \quad (8)$$

where $\dot{T}$ is the cooling rate [°C/s] and V_d is the droplet volume. Figure 7 displays our results in terms of $(NH_4)_2SO_4$ solution nucleation rates with the solid lines indicating $J(T, x)$ over the range $T_f \pm 0.5$ °C and dotted lines being 1 °C extensions of $J(T, x)$ above and below this temperature range. We note that, as expected, $J = 10^{14}$ m^3/s falls within the range $T_f \pm 0.5$ °C for most $(NH_4)_2SO_4$ concentrations with the shaded area surrounding the $J(T, x = 0)$ line indicating the limits to our precision in determining $F(T, x)$. These findings are in general agreement with previous studies, [8,12,18] although many lacked sufficient precision to establish a trend.

An alternative analysis is to fit the data set to classical nucleation rate theory (eq 2) with two free parameters: $C(T)$

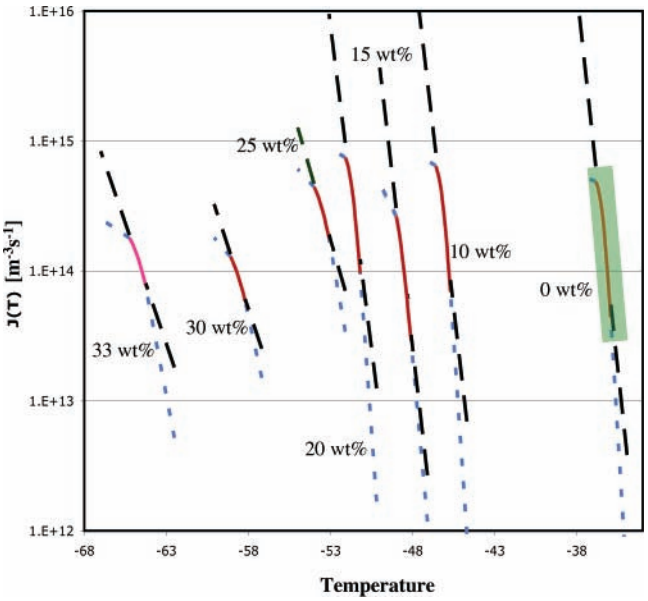

Figure 7. $(NH_4)_2SO_4-H_2O$ solution nucleation rates. Each measurement is the average of the repeat measurements at each $(NH_4)_2SO_4-H_2O$ concentration. Both the eq 2 (large-dash line) and eqs 1 and 5 (small-dash line) parametrizations agree well in the interval $J(T = T_f \pm 0.5\ °C)$ (solid line) but increasingly diverge outside this range. Note the change in $\partial J(T)/\partial T|_{T = T_f}$ with increasing concentration.

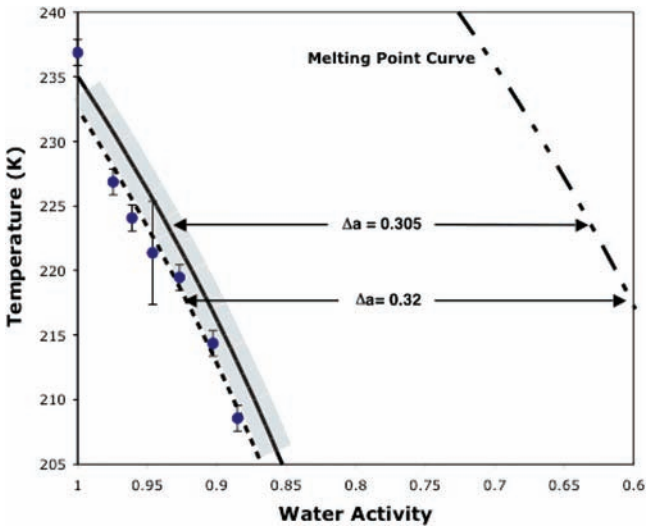

Figure 8. $(NH_4)_2SO_4-H_2O$ solution freezing temperature vs water activity. The ● indicate our average freezing temperature from repeat measurements at various concentrations with error bars as discussed in sections 2.4 and 3.3. The dash−dotted line is the melting-point curve. The solid line is the melting-point curve translated by $\Delta a = 0.305$. The dashed line is the melting-point curve translated by $\Delta a = 0.320$ which fits well our $(NH_4)_2SO_4-H_2O$ data with $a_w < 0.99$ but is inconsistent with our $a_w = 1$ data point.

and $(\Delta F_{act} + \Delta F_{germ})$. This has been done for the data ranging from $0.2 < F(T) < 0.8$ and is plotted as the long dashed lines in Figure 7. However, the precision of this fit is limited by the amplification of the scatter in the data points (even after smoothing with a three-point running average) during the conversion of $F(T)$ data to $J(T)$ data using eq 1.

These two approaches—the eq 8 parametrization and the eq 2 classical nucleation model—produce $J(T)$ curves (see Figure 7) that increasingly deviate from each other the farther they are away from the interval $J(T = T_f \pm 0.5\ °C)$ because of the differences in the two functional forms for $F(T)$. The $F(T)$ parametrization in eq 5 is asymmetric about $F(T_f)$ in the sense that for some small temperature interval ΔT one finds $F(T_f + \Delta T) = 1 - F(T_f - \Delta T)$. In contrast, eq 1 and eq 2 yield a nonsymmetric $F(T)$ with $F(T > T_f) \rightarrow 1$ with a sharp shoulder while $F(T < T_f) \rightarrow 0$ with a long, gently sloping tail. To date, the data set is not sufficiently precise to distinguish between these two forms for $F(T)$.

The dashed−dotted line in Figure 8 is the melting point curve $a_{w-m}(T)$ given by eq 4. The solid line in Figure 8 is $a_{w-f}(T) \equiv a_{w-m}(T) + \Delta a$, the freezing point curve suggested by Koop et al.[33] with $\Delta a = 0.305$. Koop et al. showed that freezing temperatures for the 18 different aqueous solutions are described well by this curve when $\Delta a = 0.305$, but the agreement between the data and this curve is not precise, and the spread in the data form a cloud of points overlaying this line with the scatter in a_w of about ±0.015. The extent of this scatter is indicated by the gray shaded region centered on $a_{w-f}(T)$. In this approach, it is necessary to convert solution concentration to a_w, and (for this 18 aqueous solution data set) Koop et al. used either the aqueous solution model of Clegg et al.[41] or assumed a_w has no temperature dependence between T_m and T_f.

The solid circles in Figure 8 are our measured mean freezing temperatures for $(NH_4)_2SO_4$. Our $(NH_4)_2SO_4$ freezing data falls outside the cloud of data from the 18 other aqueous solutions used by Koop et al. to define the $\Delta a = 0.305$ curve, and our 1σ error bars are inconsistent with the $\Delta a = 0.305$ curve. The dotted line in Figure 8 is $a_{w-f}(T)$ with $\Delta a = 0.320$, a curve

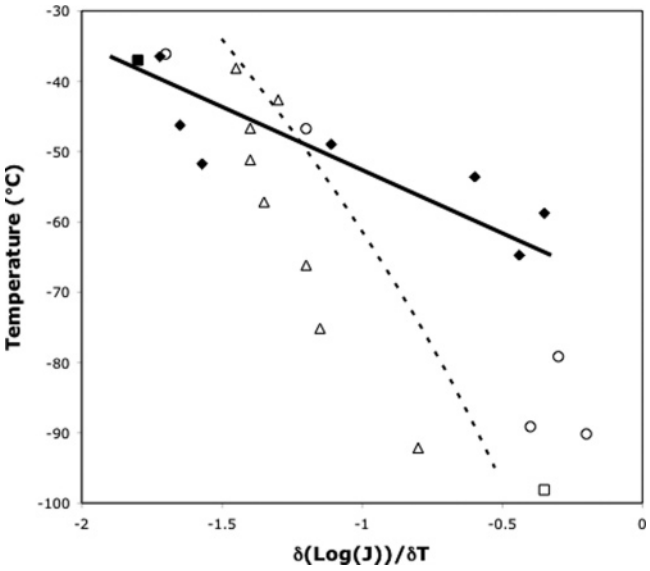

Figure 9. Nucleation rate data comparison. The ◆ indicate $\partial[\log(J)]/\partial T|_{x=const}$ for our $(NH_4)_2SO_4-H_2O$ data evaluated at $J = 10^{14}\ m^{-3}\ s^{-1}$. The solid line is the best-fit line to our $(NH_4)_2SO_4-H_2O$ data. The dashed line is $\partial[\log(J)]/\partial T|_{a_w=const}$ for the $\Delta a = 0.305$ translated melting-point curve evaluated at $J = 10^{14}\ m^{-3}\ s^{-1}$. The $\partial[\log(J)]/\partial T|_{a_w=const}$ data for LiCl (□), NH_4HSO_4 (△), and H_2SO_4 (○) are taken from Koop et al.[33] The ■ is for pure water given by classical nucleation theory calculated from the fit by Spice et al.[53]

which agrees well with our $(NH_4)_2SO_4$ data for $a_w < 0.98$ but does not fit well the pure water freezing data point at $a_w = 1$. These results indicate that, within the errors of our measurements, a TMPC does not precisely follow our $(NH_4)_2SO_4$ freezing data set.

In Figure 9, we compare $\partial[\log(J)]/\partial T|_{x=const}$ for each $(NH_4)_2SO_4$ concentration (solid points) with $\partial[\log(J)]/\partial T|_{a_w=const}$ data for LiCl, H_2SO_4, and NH_4HSO_4 (open symbols) taken from Figure 2b of Koop et al.[33] Also shown in Figure 9 (dashed line) is $\partial[\log(J)]/\partial T|_{a_w=const}$ from the $\Delta a = 0.305$ melting-line translation curve. (All results shown in Figure 9 are calculated with $J =$

10^{14} m^3/s.) The best-fit curve for the $(NH_4)_2SO_4$ data (solid line) does not precisely follow the $\Delta a = 0.305$ TMPC, but as with the deviations shown in Figure 8, more high-precision data from other solute solutions are required to evaluate the significance of this deviation.

5. Discussion

We measure $(NH_4)_2SO_4$ freezing temperatures consistent with previous OM and DSC studies,[13] and also with previous CFDC experiments,[17] despite the fact that they use an activation level of $F(T) = 0.01$. Our droplet free-fall technique practically eliminates potential substrate and emulsion-interface effects, thereby easing these concerns in previous OM and DSC results. The freezing temperatures reported here are significantly lower than those found by previous AFT studies.[14−16,18] The AFT apparatus's ability to detect 1 particle freezing in 10^6 particles and the fact that some AFT experiments define the nucleation temperature as the point where $V_d * J(T) = 1$/s may cause a 1−2 °C shift in freezing temperature depending on droplet concentration, but for the nucleation rates shown here, this does not account for the observed difference. Finally, our $(NH_4)_2SO_4$ droplets were much larger than the aerosols used in the AFT experiments, yet froze at lower temperature—which is opposite to the behavior one would expect on the basis of the size differences.[30] The differing droplet sizes used in the experiments (15−25-μm-radius droplets for our $(NH_4)_2SO_4$ data, while some of the other results discussed here were done using smaller- and larger-sized droplets) does account for some spread in the data, but predictions of the size-dependent shifts from classical nucleation theory are (a) not large enough to account for the 5+ °C freezing-point variations shown in Figure 5 and (b) not large enough to account for the disagreement between the average value for the 18 other solutes and our $(NH_4)_2SO_4$ data illustrated in Figure 8.

Our $(NH_4)_2SO_4$ results show that with increasing solute concentration the freezing temperature decreases as $\partial T_f/\partial x|_{J=\text{const}}$ [K/wt %] $= -170 + 1684x - 5310x^2$, while at the same time, the nucleation rate decreases as $\partial \log[J(T)]/\partial T|_{T=T_f} = -5.56 \times 10^{-2} T_f + 11.26$ (where T_f is in K). These trends are in general agreement with the trends expected from the melting-point translation idea and a more recent approach by Baker and Baker.[34] Also, perhaps the increasing solution viscosity and decreasing diffusivity induced by both increasing solute concentrations and the associated decrease in freezing temperature act to decrease the rate at which the initial ice crystal germ forms and grows within a liquid droplet. In addition, the process of ion rejection from the growing ice germ will be slowed by both an increased $(NH_4)_2SO_4$ concentration and a reduced freezing temperature.

Our results can speak to the questions of whether particle solidity is constant once ice initiation is detected and to what extent we detect freezing in partially frozen droplets. If significant numbers of partially frozen droplets were being detected, then one might expect the magnitude of DSL/TSL for frozen droplets to increase with decreasing temperature, and the detection of partially frozen droplets could shift $F(T)$ and T_f to higher temperature. But this is not what is observed either for pure water or for 33 wt % $(NH_4)_2SO_4$ (see Figure 2). Instead, we find that the magnitude of DSL/TSL for frozen droplets quickly saturates to the frozen particle value (0.2 for pure water and 0.25 for 33 wt % $(NH_4)_2SO_4$ by the time $F(T) = 0.3$) and no further change in the magnitude of DSL/TSL is found at lower temperatures. $F(T)$ changes from 0.1 to 0.9 (even for the most concentrated solutions) in a few centimeters corresponding to a time on the order of 0.1 s. So, although we do not know to what extent the smallest germ within a droplet is detected, it appears that the DSL/TSL signal that we detect (the proxy for freezing) saturates quite rapidly.

The deviations shown in Figures 8 and 9 between our $(NH_4)_2SO_4$ data, the TMPC, and the data for LiCl, H_2SO_4, and NH_4HSO_4 may, to some degree, be caused by the model used to convert solution concentration to a_w or to our imprecise knowledge of $a_{w-m}(T)$. Usually, the conversion of x to a_w has been done using models such as the aqueous solution model of Clegg et al.,[41,42] and there has been some discussion regarding the accuracy of the various models at low temperatures.[43−45] Indeed, this conversion is potentially problematic, since the extrapolation to low temperature of the important physical parameters has yet to be tested by comparison with low-temperature experimental results. Also, the finding that ice nucleation temperatures for aqueous solutions appear to line up so well on a single curve may, to some degree, be an artifact of the models used for converting x to a_w. The precision to which $a_{w-m}(T)$ is known remains to be established, and certainly, low-temperature measurements of important physical quantities such as solution vapor pressures are required to validate the aqueous solution models at low temperatures.

Finally, the Figure 9 analysis involves comparing two partial derivatives—one with constant a_w and the other with constant x. Formally, the difference between these two quantities is given by $\partial \log(J)/\partial T|_{a=\text{const}} = \partial \log(J)/\partial T|_{x=\text{const}} + \partial \log(J)/\partial x|_{T=\text{const}}\, \partial x/\partial T|_{a=\text{const}}$. Evaluating this difference using the Clegg model [41] and linear extrapolations of the nucleation rate data indicate the difference is negligible.

6. Atmospheric Implications

Our parametrization of $J(T, x)$ may be useful for predicting $(NH_4)_2SO_4$ freezing in cirrus cloud formation models. To compare our data with observations from field experiments monitoring the onset of cirrus cloud nucleation, we define the critical ice saturation ratio S^*_{ice} necessary to nucleate ice from preexisting aerosol

$$S^*_{ice} = P^*_{water-sol}(T_f)/P_{ice}(T_f) \quad (9)$$

where $P^*_{water-sol}(T_f)$ is the equilibrium water partial pressure of the liquid solution at freezing temperature T_f (x) associated with $(NH_4)_2SO_4$ concentration x, and $P_{ice}(T_f)$ is the vapor pressure of ice also at $T_f(x)$. A plot of T_f versus S^*_{ice} for our results shows $S^*_{ice} = 1.6$ at −64 °C. This agrees well with the findings of Bertram et al.[13] and with field measurements made at the leading edge of a wave of clouds.[5,46] These results provide evidence that low-temperature homogeneous ice nucleation could be occurring in these regions, since high water vapor concentrations are required to maintain sufficiently dilute aqueous droplets. But, a wide range of ice saturation ratios have been observed, and field observations made in other locations[46,47] find S^*_{ice} values near −53 °C to be much less than the predicted $S^*_{ice} = 1.55$ required for homogeneous freezing. Cirrus cloud chemistry is highly variable and inhomogeneous, and the extent to which cirrus clouds are produced via homogeneous and not heterogeneous processes remains an open question.[7,48−52] More field experiments that sample cirrus cloud formation conditions and more high-precision freezing experiments for other aqueous solutes are required to make further progress.

Acknowledgment. We would like to acknowledge experimental assistance from Ben Wearn, Beni Zobrist, and Robert

Seguin and helpful suggestions by Marcia Baker and Mary Laucks. This work is supported by National Science Foundation grant ATM-0323930 and grants from the University of Washington Royalty Research Fund and the University of Washington Program for Climate Change.

References and Notes

(1) Liu, H.; Wang, P. K.; Schlesinger, R. E. *J. Atmos. Sci.* **2003**, *60*, 1097.
(2) Tao, W. K. *Meteorol. Monogr.* **2003**, *29*, 107.
(3) Crutzen, P. J.; Lawrence, M. G.; Poeschol, U. *Tellus* **1999**, *51A*−*B*, 123.
(4) Lynch, D., Sassen, K., Starr, D., Stephens, G., Eds. *Cirrus*; Oxford University Press: New York, 2002.
(5) Jensen, E. J.; Toon, O. B.; Tabazadeh, A.; Sachse, G. W.; Anderson, B. E.; Chan, K. R.; Twohy, C. W.; Gandrud, B.; Aulenbach, S. M.; Heymsfield, A.; Hallett, J.; Gary, B. *Geophys. Res. Lett.* **1998**, *25*, 1363.
(6) , Martin, S. T. *Geophys. Res. Lett.* **1998**, *25*, 1657.
(7) Talbot, R. W.; Dibb, J. E.; Loomis, M. B. *Geophys. Res. Lett.* **1998**, *25*, 1367.
(8) DeMott, P. J.; Rogers, D. C.; Kreidenweis, S. M. *J. Geophys. Res.* **1997**, *102*, 19575.
(9) DeMott, P. J.; Meyers, M. P.; Cotton, W. R. *J. Atmos. Sci.* **1994**, *51*, 77.
(10) Jenson, E. J.; Toon, O. B.; Westphal, D. L.; Kinne, S.; Heymsfield, A. J. *J. Geophys. Res.* **1994**, *99*, 10421.
(11) Jensen, E. J.; Toon, O. B.; Westphal, D. L.; Kenne, S.; Heymsfield, A. J. *J. Geophys. Res.* **1994**, *99*, 19443.
(12) Sassen, K. *Bull. Am. Meteorol. Soc.* **1991**, *72*, 1848.
(13) Bertram, A. K.; Koop, T.; Molina, L. T.; Molina, M. J. *J. Phys. Chem. A* **2000**, *104*, 584.
(14) Chelf, J. H.; Martin, S. T. *J. Geophys. Res.* **2001**, *106*, 1215.
(15) Cziczo, D. J.; Abbatt, J. P. D. *J. Geophys. Res.* **1999**, *104*, 13781.
(16) Prenni, A. J.; Wise, M. E.; Brooks, S. D.; Tolbert, M. A. *J. Geophys. Res.* **2001**, *106*, 3037.
(17) Chen, Y.; DeMott, P. J.; Kreidenweis, S. M.; Rogers, D. C.; Sherman, D. E. *J. Atmos. Sci.* **2000,** *57*, 3752.
(18) Hung, H.; Malinowski, A.; Martin, S. T. *J. Phys. Chem. A* **2002**, *106*, 293.
(19) Hung, H.; Martin, S. T. *J. Geophys. Res.* **2001**, *106*, 20379.
(20) Tabazadeh, A.; Djikaev, Y. S.; Reiss, H. *Proc. Nat. Acad. Sci. U.S.A.* **2002**, *99*, 15873.
(21) Tabazadeh, A.; Djikaev, Y. S.; Harnille, P.; Reiss, H. *J. Phys. Chem. A* **2002**, *106*, 10238.
(22) Kay, J. E.; Tsemekhman, V.; Larson, B.; Baker, M.; Swanson, B. D. *Atmos. Chem. Phys. Discuss.* **2003**, *3*, 3361.
(23) Duft, D.; Leisner, T. *Atmos. Chem. Phys. Discuss.* **2004**, *4*, 3077.
(24) Kuhns, I. E.; Mason, B. J. *Proc. R. Soc. London* **1968**, *A302*, 437.
(25) Kuhns, I. E. *J. Atmos. Sci.* **1968**, *25*, 878.
(26) Hobbs, P. V.; Alkezweeny, A. J. *J. Atmos. Sci.* **1968**, *25*, 881.
(27) Wood, S. E.; Baker, M. B.; Swanson, B. D. *Rev. Sci. Instrum.* **2002**, *73*, 3988.
(28) Larson, B. H. M.S. Thesis, University of Washington, 2004.
(29) Pruppacher, H. R.; Klett, J. D. *Microphysics of Clouds and Precipitation*, 2nd ed.; Kluwer: Dordrecht, 1997.
(30) Pruppacher, H. R. *J. Atmos. Sci.* **1995**, *52*, 1924.
(31) Jeffrey, C. A.; Austin, P. H. *J. Geophys. Res.* **1997**, *102*, 25269.
(32) Mishima, O.; Stanley, H. E. *Nature (London)* **1998**, *396*, 329.
(33) Koop, T.; Luo, B.; Tsias, A.; Peter, T. *Nature (London)* **2000**, *406*, 611.
(34) Baker, M. B.; Baker, M. *Geophys. Res. Lett.* **2004**, *31*, L19102; doi: 10.1029/2004GL020483.
(35) Koop, T. *Z. Phys. Chem.* **2004**, *218*, 1231.
(36) Flagan, R. C.; Seinfeld, J. H. *Fundamentals of Air Pollution Engineering*; Prentice Hall: Englewood Cliffs, NJ, 1988.
(37) Seinfeld, J.; Pandis, S. *Atmospheric Chemistry and Physics: From Air Pollution to Climate Change*; John Wiley and Sons: New York, 1998.
(38) Turnbull, D.; Fisher, J. C. *J. Chem. Phys.* **1949**, *17*, 71.
(39) Fletcher, N. H. *The Chemical Physics of Ice*; Cambridge University Press: London, 1970.
(40) Johari, G. P.; Fleissner, G.; Hallbrucker, A.; Mayer, E. *J. Phys. Chem.* **1994**, *98*, 4719.
(41) Clegg, S. L.; Brimblecombe, P.; Wexler, A. S. *J. Phys. Chem. A* **1998**, *102*, 2137. Liquid solution model is available at http://mae.ucdavis.edu/wexler/aim.
(42) Clegg, S. L.; Ho, S. S.; Chan, C. K.; Brimblecombe, P. *J. Chem. Eng. Data* **1995**, *40*, 1079.
(43) Knopf, D. A.; Lou, B. P.; Krieger, U. K.; Koop, T. *J. Phys. Chem. A* **2003**, *107*, 4322.
(44) Clegg, S. L.; Brimblecombe, P. *J. Phys. Chem. A* **2005**, *109*, 2703.
(45) Knopf, D. A.; Lou, B. P.; Krieger, U. K.; Peter, T. *J. Phys. Chem. A* **2005**, *109*, 2707.
(46) Heymsfield, A. J.; Miloshevich, L. M.; Twohy, C.; Sachse, G.; Oltmans, S. *Geophys. Res. Lett.* **1998**, *25*, 1343.
(47) Heymsfield, A. J.; Miloshevich, L. M. *J. Atmos. Sci.* **1995**, *52*, 4302.
(48) Demott, P. J.; Cziczo, D. J.; Prenni, A. J.; Murphy, D. M.; Kreidenweis, S. M.; Thompson, D. S.; Borys, R.; Rogers, D. C. *Proc. Nat. Acad. Sci. U.S.A.* **2003**, *100*, 14655.
(49) Sheridan, P. J.; Brock, C. A.; Wilson, J. C. *Geophys. Res. Lett.* **1994**, *21*, 2587.
(50) Seinfeld, J. *Nature (London)* **1998**, *391*, 837.
(51) Karcher, B.; Strom, J. *Atmos. Chem. Phys.* **2003**, *3*, 823.
(52) Cziczo, D. J.; Murphy, D. M.; Hudson, P. K.; Thompson, D. S. *J. Geophys. Res.* **2004**, *109*, D04201; doi: 10.1029/2003JD004032.
(53) Spice, A.; Johnson, D. W.; Brown, P. R. A.; Darlison, A. G.; Saunders: C. P. R. *Q. J. R. Meteorol. Soc.* **1999**, *125*, 1637.